

A comprehensive study of type I (thermonuclear) bursts in the new transient SRGA J144459.2–604207

TAO FU,¹ ZHAOSHENG LI,¹ YUANYUE PAN,¹ LONG JI,² YUPENG CHEN,³ LUCIEN KUIPER,⁴ DUNCAN K. GALLOWAY,^{5,6} MAURIZIO FALANGA,^{7,8} RENXIN XU,^{9,10} XIAOBO LI,³ MINGYU GE,³ L.M. SONG,³ SHU ZHANG,³ AND SHUANG-NAN ZHANG³

¹Key Laboratory of Stars and Interstellar Medium, Xiangtan University, Xiangtan 411105, Hunan, P.R. China

²School of Physics and Astronomy, Sun Yat-sen University, Zhuhai 519082, People's Republic of China

³Key Laboratory of Particle Astrophysics, Institute of High Energy Physics, Chinese Academy of Sciences, 19B Yuquan Road, Beijing 100049, China

⁴SRON-Netherlands Institute for Space Research, Sorbonnelaan 2, 3584 CA, Utrecht, The Netherlands

⁵School of Physics and Astronomy, Monash University, Victoria 3800, Australia

⁶Institute for Globally Distributed Open Research and Education (IGDORE)

⁷International Space Science Institute (ISSI), Hallerstrasse 6, 3012 Bern, Switzerland

⁸Physikalisches Institut, University of Bern, Sidlerstrasse 5, 3012 Bern, Switzerland

⁹Department of Astronomy, School of Physics, Peking University, Beijing 100871, People's Republic of China

¹⁰Kavli Institute for Astronomy and Astrophysics, Peking University, Beijing 100871, People's Republic of China

ABSTRACT

We report analysis of *Insight*-HXMT observations of the newly discovered accreting millisecond pulsar SRGA J144459.2–604207. During the outburst, detected in 2024 February by *eROSITA*, the broadband persistent spectrum was well fitted by an absorbed comptonisation model. We detected 60 type I X-ray bursts in the *Insight*-HXMT medium energy (ME) data, and 37 were also detected with the low-energy (LE) telescope. By superimposing the *Insight*-HXMT/LE/ME/HE light curves of 37 bursts with similar profiles and intensities, we measured a deficit of X-rays in the 40–70 keV energy band. By analyzing the time-resolved X-ray burst spectra, we determine the mean ratio of persistent to burst flux of $\alpha = 71 \pm 7$. We estimate the average hydrogen mass fraction in the fuel at ignition, as $\bar{X} = 0.342 \pm 0.033$, and constrain the burst fuel composition as $X_0 \lesssim 0.4$. We found that 14 out of 60 X-ray bursts exhibited photospheric expansion, and thus we estimated the distance to the source as 10.03 ± 0.71 kpc. Combined with *IXPE* observations, the burst recurrence time were increasing from 1.55 to 8 hr as the local mass accretion rate decreasing, which can be described as $\Delta T_{\text{rec}} \sim \dot{m}^{-0.91 \pm 0.02}$.

1. INTRODUCTION

Type I X-ray bursts arise from unstable thermonuclear burning that occurs in low-mass X-ray binary (LMXB) systems hosting a neutron star (NS) and a low-mass companion ($M \lesssim 1M_{\odot}$; Frank et al. 1992). For detailed reviews, see Lewin et al. (1993); Lewin & van der Klis (2006), and Galloway & Keek (2021). At lower rates of local mass accretion rate ($\dot{m} \lesssim 10\%$ of the local Eddington accretion rate), typically helium-rich bursts are rapidly and powerfully triggered by the triple-alpha process, reaching a peak with ~ 1 –2 s and lasting ~ 10 –20 s. For these events the helium comes either from the helium-rich donor, or from the stable and (sometimes) complete burning of hydrogen. The burst decay time is attributed to the cooling of the NS photosphere, which leads to a gradual softening of the burst spectrum. For NS LMXBs with high mass accretion rates, type I X-ray bursts typically occur in mixed hydrogen and helium environment powered by unstable

helium ignition, where the hydrogen is accreted faster than consumed through hot CNO cycle limited by β -decays. Consequently, these bursts exhibit longer rise and decay time (see e.g., Lewin et al. 1993; Lewin & van der Klis 2006, for detailed discussions). The burst recurrence time (ΔT_{rec}) usually ranges from hours to days, depending on the accretion rate and the composition of the accreted material (see e.g., Galloway & Cumming 2006). The relation, $\Delta T_{\text{rec}} \sim \dot{m}^{-1}$, has been found in systems such as the “clocked” bursters GS 1826–24 and 1RXS J180408.9–342058, and two accreting millisecond X-ray pulsars (AMXPs) SAX J1748.9–2021 and MAXI J1816–195 (Galloway et al. 2004; Goodwin et al. 2019; Li et al. 2018; Wang et al. 2024).

The X-ray burst spectrum can be described in terms of blackbody radiation with temperature of $kT_{\text{bb}} \approx 0.5$ –3 keV. From the time-resolved burst spectral studies, the flux of type I X-ray bursts can reach the Eddington limit, and the radiation pressure exceeds the gravitational po-

tential on the NS surface, leading to photosphere radius expansion (PRE; Lewin et al. 1993). PRE bursts are usually used as standard candles to determine the distance to the source phenomenologically (Kuulkers et al. 2003). The interactions between burst radiation and the surrounding accretion disk have been observed as the enhancement of persistent accretion due to the Poynting-Robertson drag (Worpel et al. 2013, 2015; Ballantyne & Strohmayer 2004; Keek et al. 2014; Zhao et al. 2022; Lu et al. 2023), the deficient hard X-ray emission due to corona cooling, and the accretion disk reflection (Chen et al. 2012; Ji et al. 2013; Chen et al. 2018, 2019; Speicher et al. 2024; Yu et al. 2024; Lu et al. 2024).

SRGA J144459.2–604207 was discovered on 21 February 2024 by the Mikhail Pavlinsky ART-XC telescope survey mission (Molkov et al. 2024). Follow-up observations revealed the source is a new AMXP with a spin period of 447.8 Hz, and an orbital period of ~ 5.2 hr (Ng et al. 2024; Li et al. 2024). Several X-ray instruments have detected many X-ray bursts from SRGA J144459.2–604207, i.e., NICER (five bursts, Ng et al. 2024; Ray et al. 2024), Swift/XRT (one burst, Chandra 2024), MAXI/GSC (one burst, Negoro et al. 2024), NinjaSat (three bursts, and first two bursts are the same as bursts #36 and #40 in *Insight*-HXMT, Takeda et al. 2024), Chandra (one burst, Illiano et al. 2024), INTEGRAL (Sguera & Sidoli 2024; Sanchez-Fernandez et al. 2024), and *IXPE* (52 bursts and 18 of them also in the *Insight*-HXMT burst sample, Papitto et al. 2024). These observations show that the burst recurrence time varied between 1.6–8.0 hr as the persistent count rate decreased. The *IXPE* observations found the relation between the recurrence and the persistent count rate $t_{\text{rec}} \sim C^{-0.8}$ (Papitto et al. 2024).

In this paper, we reported the X-ray burst properties of the AMXP SRGA J144459.2–604207 using the *Insight*-HXMT observations. In Sect. 2, we described the data reduction procedure of *Insight*-HXMT. In Sect. 3, we introduced the characteristics of X-ray burst light curves, the persistent emission, and time-resolved spectra for the X-ray bursts. We discussed the results in Sect. 4.

2. OBSERVATION

The Insight Hard X-ray Modulated Telescope (*Insight*-HXMT; Zhang et al. 2020) has three collimating telescopes, the Low Energy X-ray telescope (LE; Liao et al. 2020), the Medium Energy X-ray telescope (ME; Guo et al. 2020), and the High Energy X-ray telescope (HE; Liu et al. 2020), which have effective areas of 400, 900, and 5000 cm², respectively, covering the broadband energy range of 1–250 keV. After SRGA J144459.2–604207

was confirmed as an AMXP, we proposed ToO observations using *Insight*-HXMT (PI: Zhaosheng Li). *Insight*-HXMT conducted 53 observations of SRGA J144459.2–604207 between 23 February and 15 March 2024, with a total exposure time of 691 ks. We processed and analyzed the data using the *Insight*-HXMT Data Analysis Software (HXMTDAS) v2.06. The light curve, source and background spectra for LE, ME, and HE were extracted using the tool, *lepipeline*, *mepipeline*, and *hepipeline*, respectively. We screened the data according to the standard criteria: the offset angle from the pointing direction $< 0.04^\circ$; the pointing direction above Earth $> 10^\circ$; and the cut-off rigidity value > 8 GV. The net exposures obtained from LE, ME, and HE were 104, 123, and 129 ks, respectively.

We note that the default good time interval (GTI) selection criteria for LE and ME are very conservative due to a light leak (Liao et al. 2020), and many X-ray bursts were missed. We followed the same procedure used for observations of MAXI J1816–195 (Chen et al. 2022a) to extract the light curves and spectra without filtering on GTIs, to obtain a complete sample of bursts from SRGA J144459.2–604207. The light curves of LE, ME, and HE data are extracted with a time bin of 1 s. In Figure 1, we show the effect of such a treatment as an example, in which the Obs. id. P061437300103 contains bursts #4 and #5. These two bursts were missed in the LE and ME light curves generated by the standard GTI filtering criteria. When *Insight*-HXMT passed through the South Atlantic Anomaly, burst-like fluctuations that could be caused by sharp changes in the background were excluded.

We also processed the *IXPE* data of SRGA J144459.2–604207 (see also Papitto et al. 2024). For each detector unit, the 1-s binned light curves were extracted from a 100'' circle region around the source position. We identified the onset time of 52 type I X-ray bursts. The pre-burst count rates of these bursts were calculated, which were used to convert to the persistent flux (see Sect. 4.3).

3. RESULTS

3.1. Burst light curves

We found 60 type I X-ray bursts in the ME data, and 37 of them were also detected in LE data. No bursts were apparent in HE data, covering 25–250 keV, likely because the burst spectra were too soft. From 1 s binned ME light curves, we defined a time interval between 70 and 20 s before the burst peak as the pre-burst emission. At the end of the pre-burst, we defined the time when the count rate was 105% of the average count rate of the pre-burst emission as the burst onset time. We

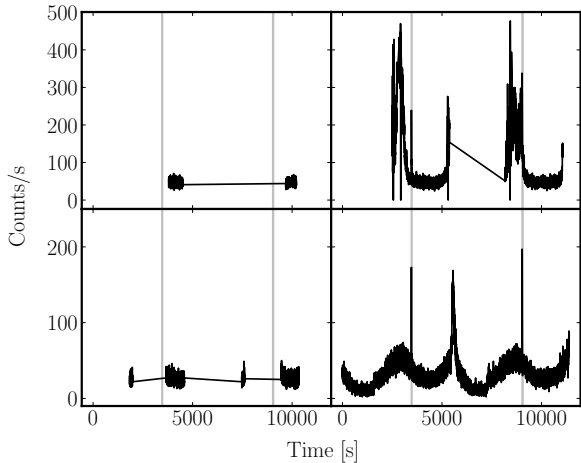


Figure 1. The light curves from Obs. id. P061437300103, which contains bursts #4 and #5. The top left and right panels show the LE light curves for standard processing and without filtering any GTI, respectively. The lower left and right panels are the ME light curves for standard processing and without filtering any GTI, respectively. The gray lines represent the time of two bursts occurrence.

found that the ME and LE bursts had almost the same onset time, except for burst #5, for which the LE light curve was ~ 2 s ahead of ME. We subtracted the average pre-burst count rate for both LE and ME burst light curves, as shown in Figure 2. The profiles of the LE and ME light curves for 60 bursts were compared and it was found that the ME light curve profiles in the 10–35 keV range were quite similar. The burst light curves reached a rough plateau with peak count rates of ~ 130 cts/s and duration of 7–10 s after a fast rise time of 2–3 s, followed by an exponential decay to the pre-burst level. The LE burst light curves had a higher peak count rate, ~ 180 cts/s, than the ME bursts, but the profiles are otherwise quite similar in shape.

We defined the recurrence time as the duration between the burst onset of two successive bursts by incorporating the bursts from *IXPE*, *NinjaSat*, and *INTEGRAL*, and list the values in Table 1. Some bursts have recurrence times that are significantly longer than others immediately before or after, which implies that some bursts may have been missed due to gaps in the data. We obtained the true recurrence time by dividing the observed recurrence time by the integer $N + 1$, where N is the number of missed bursts. For instance, the ΔT_{rec} for burst #41 is 4.49 hours, and by comparing with bursts #40 and #42, it is suspected that one burst might be missed. From the *IXPE* burst sample, there was a burst on MJD 60368.10542, which perfectly filled the gap between bursts #40 and #41, confirming

the reliability of our method for obtaining the true recurrence time. We found that as the persistent emission decreases, the recurrence time for the bursts observed with *Insight*-HMXT increased from 1.55 to 3.65 hr.

3.2. Spectral analysis of the persistent emission

We fitted the simultaneous *Insight*-HXMT LE, ME and HE spectra using XSPEC version 12.12.1 (Arnaud 1996). The *Insight*-HXMT spectra were grouped by a factor of 5 using the tool `grppha`. All uncertainties of the spectral parameters are provided at a 1σ confidence level for a single parameter.

We adopted the energy ranges of 2–10 keV, 8–20 keV, and 30–100 keV for *Insight*-HXMT LE, ME, and HE spectra, respectively. We fit all the spectra by using the thermally Comptonized continuum, `nthcomp`, modified by the interstellar absorption described by the model, `tbabs`. The full model is `tbabs × nthcomp` in XSPEC. The blackbody seed photons were assumed for `nthcomp`.

To account for cross-calibration uncertainties between different instruments, a multiplication factor, `constant` in XSPEC, is included in the fits. The factor is fixed at unity for *Insight*-HXMT/LE and freed for *Insight*-HXMT/ME/HE. The other free parameters are: the asymptotic power-law photon index, Γ , the electron temperature, kT_e , the temperature of the soft seed photons, kT_{bb} , the type of seed photons (the blackbody seed photons are assumed), the normalization, and the hydrogen column density, N_{H} . These parameters of ME and HE were tied with the same values for LE.

The fitted parameters throughout the outburst are shown in Figure 3. All spectra can be well fitted with $\chi^2_{\nu} < 1.25$. We calculated the unabsorbed bolometric flux in the 0.5–250 keV range by using the tool `cflux`. The temperature of seed photons was around 0.4 keV. The hydrogen column density did not change much, and the mean value is $(1.87 \pm 0.18) \times 10^{22} \text{ cm}^{-2}$, thus it was fixed during the fitting. The asymptotic power-law photon index was in the range 1.9–2.2, which explains the visibility of hard X-ray emissions during the whole outburst. The electron temperature was in the range 10–25 keV. The bolometric flux decreased from a peak value of $4.59 \times 10^{-9} \text{ erg cm}^{-2} \text{ s}^{-1}$ to $2.36 \times 10^{-9} \text{ erg cm}^{-2} \text{ s}^{-1}$ at MJD 60373.3.

3.3. Time-resolved burst spectral analysis

We performed time-resolved spectral fits on each burst observed with *Insight*-HXMT. Bursts # 35 and # 45 occurred during a period of unusually high background levels, therefore their burst spectra were polluted and ignored in the burst spectral analysis. So, we analyzed 58 type I X-ray bursts from the *Insight*-HXMT observations. For ME bursts, we extracted the spectra with an

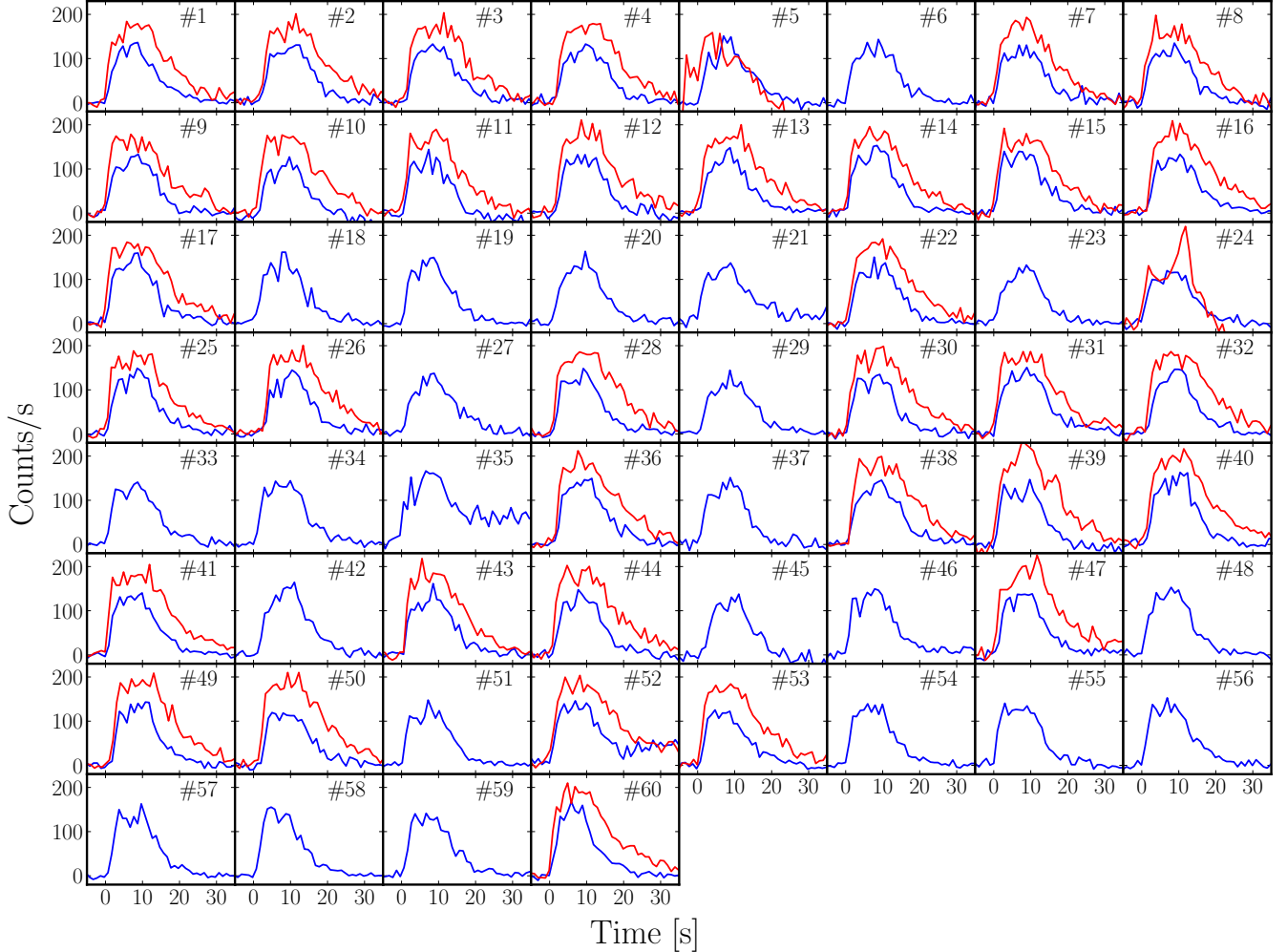


Figure 2. Light curve of the 60 X-ray bursts from SRGA J144459.2–604207 observed with Insight–HXMT. The red and blue lines represent the light curves of the LE (2–10 keV) and ME (10–35 keV) bursts respectively. The persistent LE and ME count rates are subtracted independently. Light curves were relative to the burst onset time.

exposure time of 1–4 s to ensure at least 100 counts in each spectrum. We used the same time intervals to extract LE burst spectra if the LE data are available. The burst spectra were grouped using `ftool grapha` with a minimum of 10 counts per channel.

To fit the burst spectra, we used an absorbed blackbody model, `TBabs×bbodyrad`. We regarded the pre-burst spectra as background, which was assumed invariant during the bursts. The spectral parameters include the blackbody temperature kT_{bb} and normalization (R_{km}^2/D_{10}^2), where R_{km} is the apparent burst radius in km, and D_{10} the distance to the source in units of 10 kpc. For each burst, we fixed the hydrogen column density at $1.87 \times 10^{22} \text{ cm}^{-2}$. For the joint LE and ME spectral fitting, to account for the instrumental calibration, a constant was added to the model, which was fixed at 1 for LE, and set free for ME. The model fitted most of the burst spectra well with $\chi^2_{\nu} \sim 0.5 - 1.5$.

For some burst spectra with large χ^2_{ν} , we used instead the variable persistent flux method to improve the fitting. We assumed that only the normalisation of the persistent component can change during bursts, and the spectral shape remains constant. Then only the instrumental background was subtracted. The model is `constant×TBabs×(bbodyrad+fa×nthcomp)`. The `nthcomp` accounts for the persistent emission during the burst, and the parameters were fixed to the best-fitted values for each observation, listed in Table 1. The parameter f_a is a free scaling factor that is used to account for the persistent emission variation during the burst. $f_a = 1$ means that the normalisation of the persistent emission during the burst is unchanged compared to the value before the burst. By fitting all the burst spectra, we found that the variable persistent flux model can improve the fit, but most of parameters are consistent with the blackbody model at 1σ confidence level. See

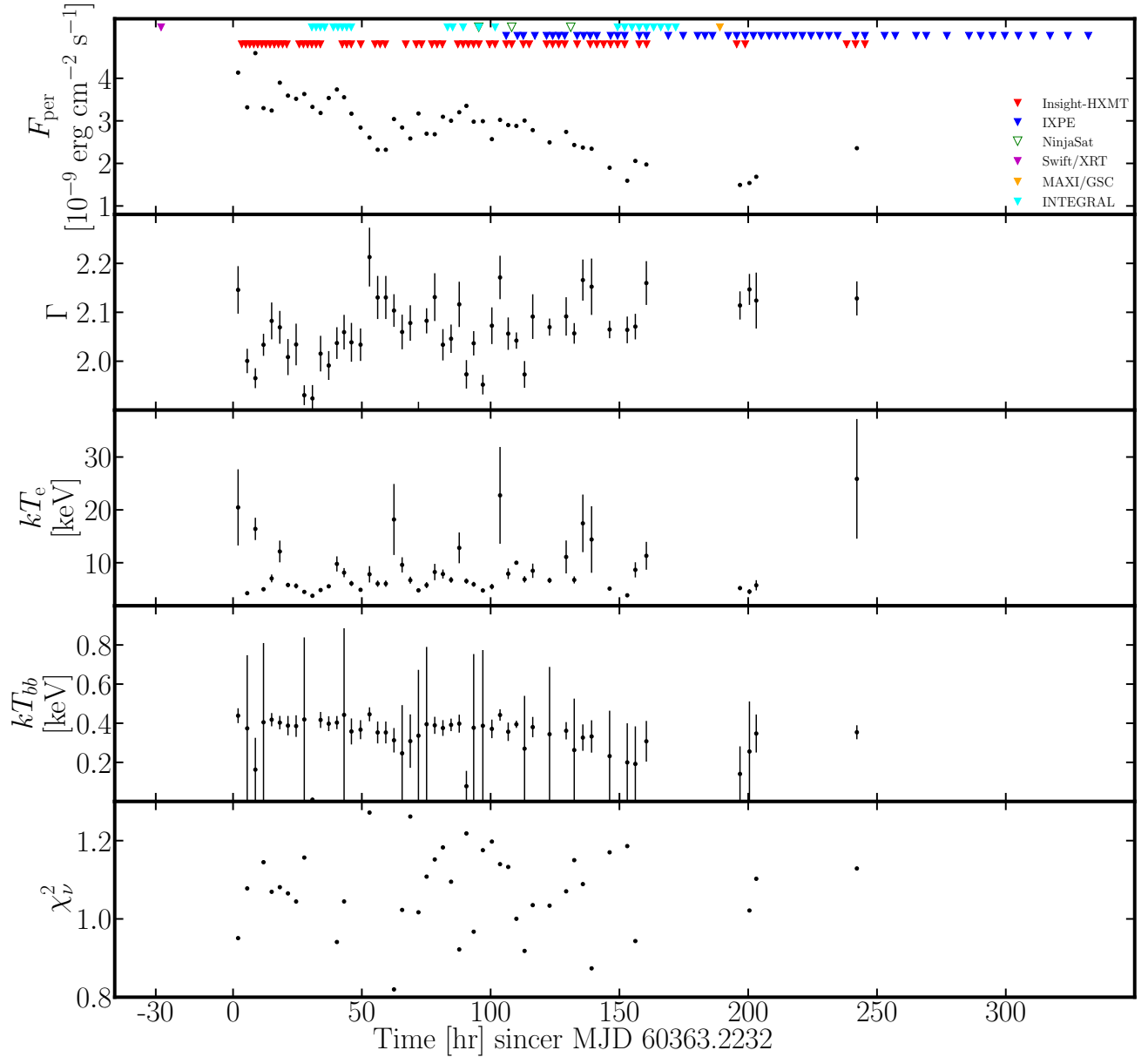


Figure 3. The evolution of persistent spectrum with *Insight*-HXMT data with the bolometric flux calculated in 0.5–250 keV. The black points represent the parameters of model `constant×TBabs×nthcomp` with the fixed centroid. The onset time of all type I bursts are marked as triangle in the top panel.

e.g. Figure 4 for burst #10, which has the most significant improvement. In this work, we only reported the results from the blackbody model.

Based on the time-resolved spectra, we found that 14 bursts, including bursts #2, #5, #7, #8, #13, #18, #19, #22, #28, #42, #51, #52, #53, and #55 exhibit PRE, see Figure 5. For these 14 bursts, the blackbody radius increased at the burst start and reached a maximum at around 10 km (for $d = 10.03$ kpc, see Sect. 4.2). When the photosphere fell back to the NS surface, the color temperature increased to its peak at ~ 3 keV and the apparent radius decreased to its local

minimum, which corresponds to the “touchdown” moment. Afterwards, the color temperature decreased and apparent radius was maintained at a constant level of 6.22 ± 1.53 km,

All bursts were characteristic of blackbody flux with fast rising and exponential decaying, and spectral softening after the burst peak. We calculated the burst fluence, f_b , from the sum of the product of blackbody flux and its exposure time. From the above fitted parameters, the burst decay timescale is obtained by $\tau = f_b/F_{\text{peak}}$, where F_{peak} is the peak flux. All burst parameters are listed in Table 1.

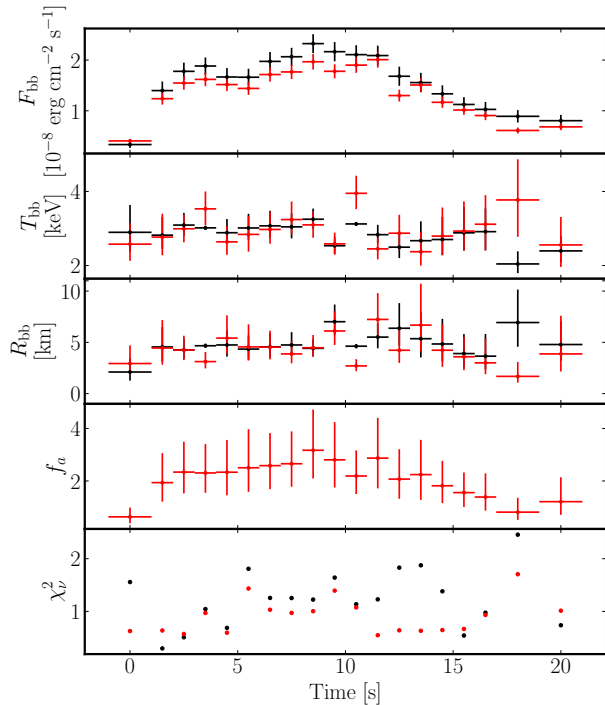


Figure 4. Time-resolved spectroscopy using the variable persistent flux model (red dot) and the blackbody model (black dot) for joint LE and ME spectra of burst #10. The panels are, from top to bottom, the bolometric burst flux F_{bb} ; blackbody temperature T_{bb} ; blackbody radius R_{bb} ; multiplicative term for the persistent flux f_a (only relevant for the variable persistent flux method); and fit statistic, χ^2_{ν} .

4. DISCUSSION

In this paper, we analyzed the broadband *Insight*-HXMT observations of the newly-discovered AMXP SRGA J144459.2–604207 during its 2024 outburst. We found 60 type I (thermonuclear) X-ray bursts from *Insight*-HXMT/ME, and 37 of them were also observed by *Insight*-HXMT/LE. The persistent spectra in the energy range 2–150 keV can be well fitted with the `tbabs×nthcomp` model. Most of bursts showed a similar profile, a fast rise in 2–3 s followed by a plateau lasting 7–10 s and then an exponential decay.

We performed a detailed time-resolved spectral analysis of 58 type I X-ray bursts. We found that the variable persistent flux model did not improve the residuals of the `tbodyrad` model significantly, which may be caused by the limited signal-to-noise ratio of the spectra. By stacking the light curves, as reported in Sect. 4.1 we measured a deficit in the HE light curve. From the time-resolved spectra, 14 bursts showed PRE, and the burst composition and source distance were determined in Sect. 4.2. In Sect. 4.3, we discussed the relation between the burst recurrence time and the local mass accretion rate. We

compared the calculated recurrence time with the actual recurrence time, which further reconfirms the fuel composition of hydrogen and helium.

4.1. The stacking of burst light curves

The spectra of LMXBs, including both black hole (BH) and NS X-ray binaries (XRBs), are generally composed of soft/thermal (e.g., blackbody or disk blackbody) and hard/Comptonized components. The hard X-rays in XRBs are produced via inverse Compton scattering of the soft photons off the hot electrons in the corona. The burst spectrum is usually modeled by a blackbody model of characteristic temperature in 0.5–3 keV. The burst emission can reach L_{Edd} and dominates the total emission at energies well below ~ 30 keV, above which the persistent emission from the purported corona dominates. Therefore, the *Insight*-HXMT/HE observations in the 40–70 keV energy band allow us to study the possible effects of the bursts on the corona.

The LE and ME burst light curves have a similar profile, which can be stacked to probe the effects of burst-induced corona cooling with improved statistics. We combined the LE, ME, and HE light curves for all the bursts in the 2–10, 10–35, and 40–70 keV energy ranges, respectively, between $-50 \sim 100$ s relative to the burst onset time (following Chen et al. 2012). As shown in Figure 6, the HE flux dropped at the same time that LE and ME detected an increase in burst flux. As the burst decays, the HE flux returned to pre-burst levels. The mean HE pre-burst rate was ~ 126 cts/s, includes a background contribution of ~ 121 cts/s and persistent (source) contribution of ~ 5 cts/s. At the peak of the burst, the HE rate decrement reaches a maximum of $\sim 6 \pm 1.5$ cts/s corresponding to significance of 4σ , which was $\sim 120 \pm 30\%$ of the total persistent flux in 40–70 keV. Chen et al. (2022b) and Ji et al. (2024) proposed that the deficit fraction might be systematically lower for pulsating compared to non-pulsating LMXBs. However, for SRGA J144459.2–604207, the reduced persistent emission in its hard energy band cannot give a reasonable deficit fraction.

A cross-correlation analysis was carried out between the ME light curve in 10–35 keV and the HE light curve in 40–70 keV with a bin size of 1 s. The HE light curve was anti-correlated with the ME light curve, with the minimum value at 0.81 ± 0.58 s, which indicates the hard X-ray deficit lagged behind the burst emission.

Similar phenomena have also been reported in the type I X-ray bursts of IGR J17473–2721 (Chen et al. 2012), Aql X–1 (Chen et al. 2013), 4U 1636–536 (Chen et al. 2018) and MAXI J1816–195 (Chen et al. 2022b). The deficit in hard X-rays during bursts is explained as

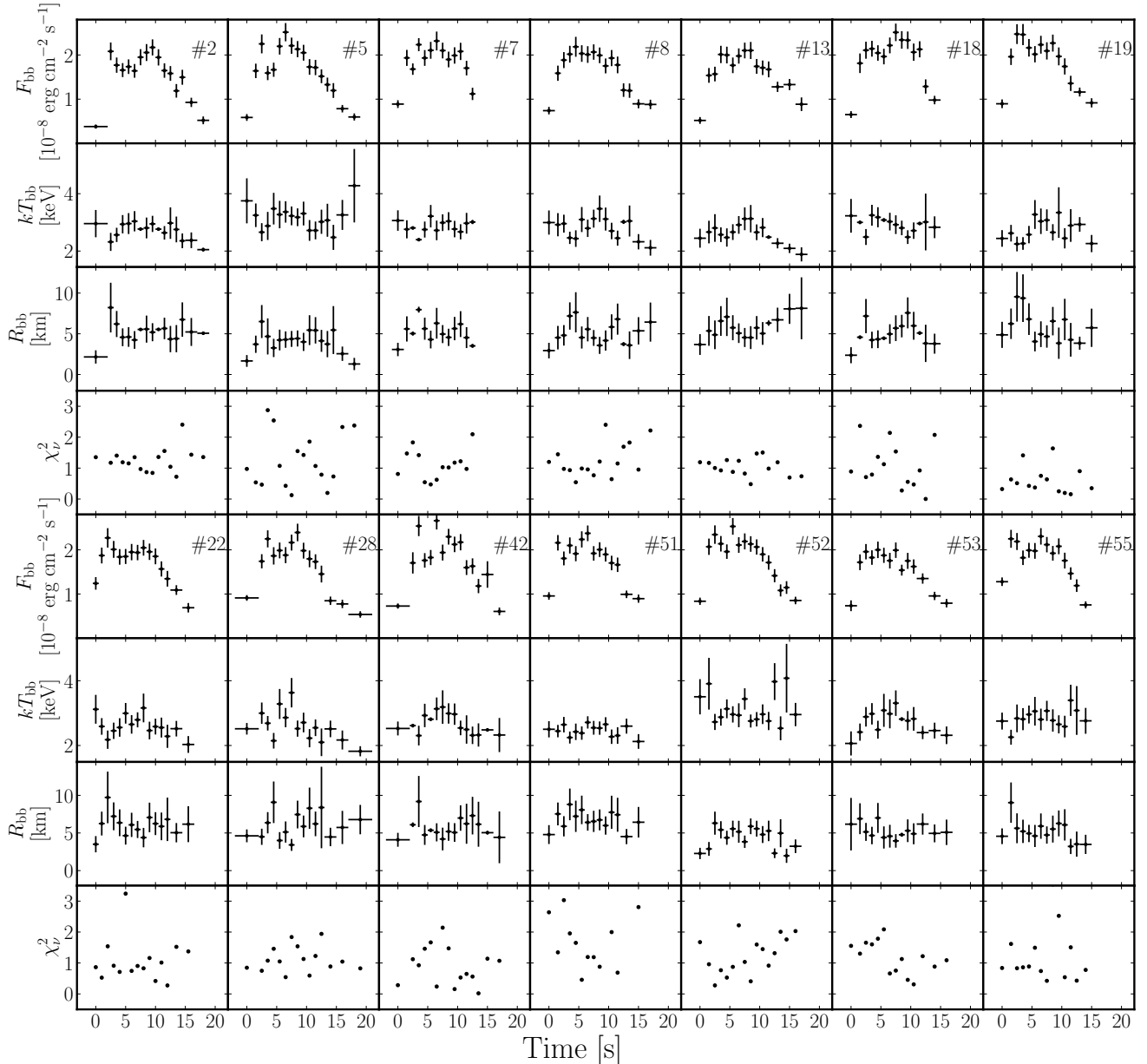


Figure 5. Time-resolved spectroscopy using the `TBabs` \times `bodyrad` for PRE bursts #2, #5, #7, #8, #13, #18, #19, #22, #28, #42, #51, #52, #53, and #55. For each panel, from top to bottom, we exhibit the burst bolometric flux, F_{bb} ; the blackbody temperature, kT_{bb} , the blackbody radii, R_{bb} , which were calculated using a distance of 10.03 kpc, and the goodness of fit per degree of freedom, χ^2_ν , respectively.

cooling of the corona by the burst, which provides an intense shower of the soft X-rays to cool the hot corona via Comptonization process. When bursts do not occur, the corona cooling is driven by the soft photons from the disk or boundary layer. When bursts occur, their soft photons overwhelm those from the disk and provide additional cooling in a typical timescale of tens of seconds. The anti-correlation between hard and soft X-rays suggests that the corona can be cooled down and recovers quite fast within a few seconds. Such a short

timescale for the corona recovery is inconsistent with the disk evaporation model in which the formation of a corona is driven and energized by the disk accretion with a typical timescale of days. As previously discussed by Zhang et al. (2000) and Zhang (2007), an alternative magnetic field re-connection model can explain such rapid evolution. Magnetic field reconnection in the inner disk region can release the kinetic energies in the rotating disk to heat the corona with the Keplerian or-

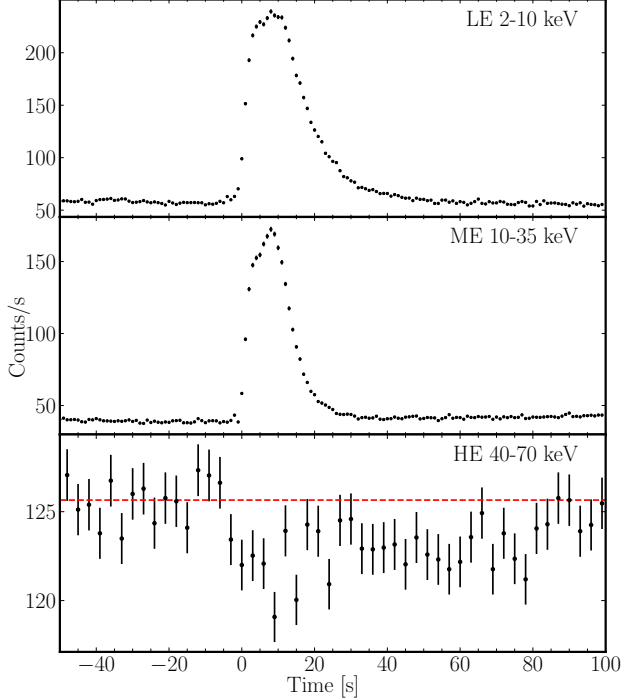


Figure 6. From top to bottom panels, we show the LE, ME, and HE light curves during bursts in 2–10 keV, 10–35 keV, and 40–70 keV, respectively. The binsize is 1 s for LE and ME, 3 s for HE.

bitual timescale of milliseconds, comparable to the case of SRGA J144459.2–604207.

4.2. The source distance and X-ray burst fuel

From the persistent and burst spectral results, we can determine the burst fuel and source distance. We calculated the α factor to verify the burst fuel composition,

$$\alpha = \frac{\Delta T_{\text{rec}} F_{\text{per}}}{f_{\text{b}}}, \quad (1)$$

which is the ratio between the persistent to the burst fluence. From the average values of burst fluence, persistent flux, and ΔT_{rec} , we found the average $\alpha = 71 \pm 7$, which is consistent with the mixed hydrogen and helium fuel. We can also calculate the α as

$$\alpha = \frac{Q_{\text{grav}} \xi_{\text{b}}}{Q_{\text{nuc}} \xi_{\text{p}}} (1+z), \quad (2)$$

where $Q_{\text{grav}} = c^2 z(1+z) \approx GM_{\text{NS}}/R_{\text{NS}}$, ξ_{b} and ξ_{p} account for the anisotropy of burst and persistent emission, respectively. The gravitational redshift at the photosphere $1+z = (1 - 2GM_{\text{NS}}/Rc^2)^{-1/2} = 1.259$ for $M_{\text{NS}} = 1.4M_{\odot}$, and $R = R_{\text{NS}} = 11.2$ km. For a fuel layer consisting of mixed hydrogen and helium, Q_{nuc} depends on the mean hydrogen fraction, \bar{X} , at ignition,

which is given by (Goodwin et al. 2019)

$$Q_{\text{nuc}} \approx 1.31 + 6.95\bar{X} - 1.92\bar{X}^2 \text{ MeV nucleon}^{-1}. \quad (3)$$

By substituting the linear expression in Equation (3) for simplicity, it can be estimated (Galloway et al. 2022)

$$\bar{X} = z \frac{155 \xi_{\text{b}}}{\alpha \xi_{\text{p}}} - 0.223. \quad (4)$$

We assumed that the anisotropy factors ξ_{b} and ξ_{p} are both unity. So we obtained the mean $\bar{X} = 0.342 \pm 0.033$.

If we assume the observed peak flux of PRE bursts corresponding to the Eddington limit, the distance to the source can be measured as,

$$\begin{aligned} d &= \left(\frac{L_{\text{Edd}, \infty}}{4\pi \xi_{\text{b}} F_{\text{pk, RE}}} \right)^{1/2} \\ &= 8.83 \left(\frac{\xi_{\text{b}} F_{\text{pk, RE}}}{3 \times 10^{-8} \text{ erg cm}^{-2} \text{ s}^{-1}} \right)^{-1/2} \left(\frac{M_{\text{NS}}}{1.4M_{\odot}} \right)^{1/2} \\ &\times \left(\frac{1+z}{1.259} \right)^{-1/2} (1+X)^{-1/2} \text{ kpc}, \end{aligned} \quad (5)$$

where $F_{\text{pk, PRE}}$ is the mean peak flux (2.33 ± 0.17) $\times 10^{-8} \text{ erg cm}^{-2} \text{ s}^{-1}$ of 14 PRE bursts, X is the mass fraction of hydrogen in the atmosphere. The effective redshift measured at the peak of a PRE burst may be lower than the value at the NS surface, while the photosphere is expanded during the radius expansion episode (i.e., $R \geq R_{\text{NS}}$). Evidences suggests that even if the atmosphere contains hydrogen, the hydrogen-rich material is typically blown off during the PRE phase, exposing the underlying helium layer (see e.g., Galloway et al. 2006; Bult et al. 2019; Guichandut & Cumming 2023). Then we obtained the distance $d = 10.03 \pm 0.71$ kpc for $X = 0$. Hereafter, we use 10.03 kpc as the distance to the source.

We selected three pairs of bursts for further analysis; two observed with *Insight-HXMT* (#4 & 57 in Table 1), and an additional pair observed by *IXPE*, with recurrence times 1.53, 3.29, and 7.91 hr, respectively. For each pair we calculated the α value (equation 4.2), based on the estimated persistent flux at the time of the burst, and the burst fluence. We then inferred the average H-fraction in the burst fuel via estimates of Q_{nuc} and \bar{X} , as for the average quantities above. We also incorporated the effects of the persistent and burst flux anisotropy, using the CONCORD suite of tools following Galloway et al. (2022). We adopted the inclination inferred by Papitto et al. (2024) from the phase-resolved Stokes parameters, of $i = (74.1_{-6.3}^{+5.8})^\circ$. For a roughly solar metallicity ($Z_{\text{CNO}} = 0.02$) the fuel H-fraction, X_0 , is significantly below solar (Fig. 7). In fact, for the most

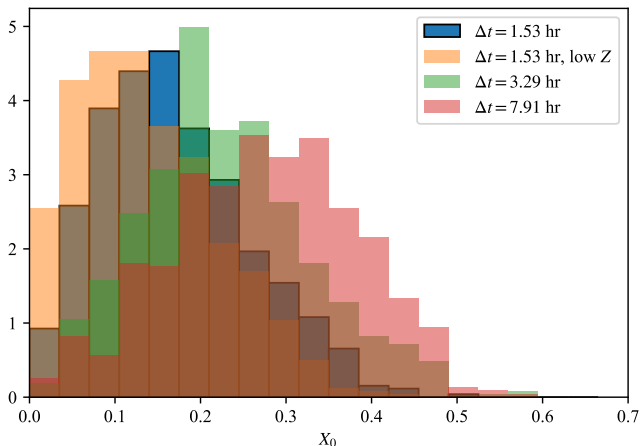


Figure 7. Inferred probability density function of the H-fraction X_0 for the burst fuel, based on three pairs of bursts with different recurrence times. The shortest pair of bursts provides the most stringent constraints on X_0 , strongly suggesting the burst fuel is H-deficient. For the same pair we also plot the inferred X_0 for low CNO metallicity, $Z_{\text{CNO}} = 0.005$ rather than the roughly solar value of 0.02.

constraining pair of bursts (with $\Delta t = 1.53$) $X_0 \lesssim 0.4$. Reducing Z_{CNO} shifts this distribution to even lower values of X_0 , so we consider the upper limit robust, unless the CNO metallicity is instead substantially *super*-solar.

4.3. The burst recurrence time

We found that the burst recurrence time increased from 1.55 to 3.65 hr as the persistent flux decreasing. In following, we verified the relation between recurrence time and local accretion rate. The local accretion rate is determined via (Galloway et al. 2008),

$$\begin{aligned} \dot{m} &= \frac{L_{\text{per}}[1+z]}{4\pi R_{\text{NS}}^2 (GM_{\text{NS}}/R_{\text{NS}})} \\ &\approx 6.7 \times 10^3 \left(\frac{F_{\text{per}}}{10^{-9} \text{ erg cm}^{-2} \text{ s}^{-1}} \right) \left(\frac{d}{10 \text{ kpc}} \right)^2 \\ &\times \left(\frac{M_{\text{NS}}}{1.4M_{\odot}} \right)^{-1} \left(\frac{1+z}{1.259} \right) \left(\frac{R_{\text{NS}}}{11.2 \text{ km}} \right)^{-1} \text{ g cm}^{-2} \text{ s}^{-1}, \end{aligned} \quad (6)$$

where F_{per} is the persistent flux. In Fig. 8, we show the evolution of peak flux, the total energy releasing, and α as a function of \dot{m} . We found that all these parameters were almost unchanged from the peak to the end of outburst, same as shown from burst light curves. We estimated the ignition depth at the onset of the burst with the equation

$$y_{\text{ign}} = \frac{4\pi f_{\text{b}} d^2 (1+z)}{4\pi R_{\text{NS}}^2 Q_{\text{nuc}}}, \quad (7)$$

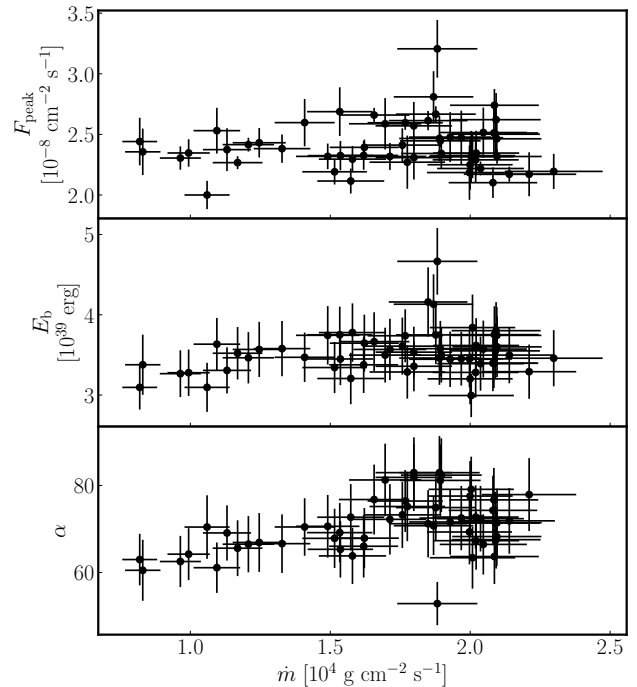


Figure 8. The burst parameters, the peak flux, the total released energy, and α , from top to bottom panel, related to the local mass accretion rate. The α of the last three bursts are not shown due to inaccurate of the pre-burst persistent flux.

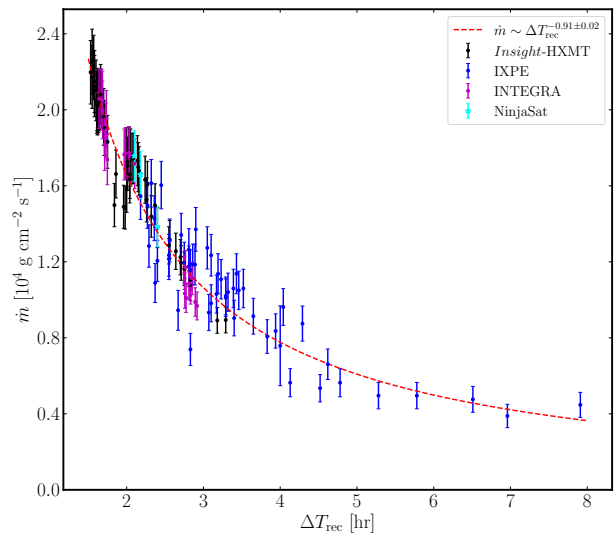


Figure 9. The relation between the recurrence time and local mass accretion rate. The red dashed line represents the best-fitted power-law $\dot{m} \sim \Delta T_{\text{rec}}^{-0.91 \pm 0.02}$.

which are listed in Table 1.

Since the complete burst sample was obtained without GTI filtering, the pre-burst persistent emission flux for some bursts could not be obtained by the standard spectral fitting process. By applying the UnivariateSpline method, we interpolated the persistent flux from Sect. 3.2 to obtain the pre-burst persistent emission. Then, the local mass accretion rates for bursts from *Insight*-HXMT, *IXPE*, and INTEGRAL, are calculated. Since the uncertainties of recurrence time are much smaller than the measured value, we only considered the uncertainties of the local mass accretion rate. The observed recurrence time increased with decreasing of \dot{m} as $\dot{m} \sim \Delta T_{\text{rec}}^{-1.09 \pm 0.03}$, or inversely $\Delta T_{\text{rec}} \sim \dot{m}^{-0.91 \pm 0.02}$, see Figure 9. We note that the X-ray bursts detected by *IXPE* showed a similar trend of $\Delta T_{\text{rec}} \sim C^{-0.8}$, even though the direct measurement of local mass accretion rate was difficult (Papitto et al. 2024). By assuming that the bursts were occurred under the same physical conditions, the accreted matter between two bursts should be the same. Therefore, it is expected that the local accretion rate, \dot{m} , is related to the burst recurrence time by $\Delta T_{\text{rec}} \sim \dot{m}^{-1}$ (Li et al. 2018). The index of -0.91 in SRGA J144459.2-604207 slightly deviates from the expectation, which may be caused by the fluctuations of the persistent flux observed by *Insight*-HXMT.

5. SUMMARY

We detected 60 type I X-ray bursts from SRGA J144459.2-604207 with *Insight*-HXMT observations. The persistent spectra of all bursts were well fitted by TBabs×nthcomp, showing a similar spectral shape. A shortage of hard X-rays in the 40–70 keV range was detected by stacking the *Insight*-HXMT light curves of 37 type I X-ray bursts with similar profiles and count rates. We analyzed the time-resolved spectra of all bursts and found that 14 of 60 type I X-ray bursts are PRE bursts. We obtained a distance of 10.03 ± 0.71 kpc for this source. Based on the depth of ignition, the local accretion rate, and the recurrence time, we proposed that these X-ray bursts were ignited in a mixture of hydrogen and helium environment.

1 We appreciate Celia Sanchez Fernandez for shar-
 2 ing the onset time of INTEGRAL bursts. This work
 3 was supported the Major Science and Technology Pro-
 4 gram of Xinjiang Uygur Autonomous Region (No.
 5 2022A03013-3). Z.L. and Y.Y.P. were supported by Na-
 6 tional Natural Science Foundation of China (12103042,
 7 U1938107, 12273030). This work made use of data from
 8 the *Insight*-HXMT mission, a project funded by China
 9 National Space Administration (CNSA) and the Chinese
 10 Academy of Sciences (CAS).

Table 1. Table 1

NO.	Obs id ^a	Burst Onset	F_{peak}	f_b	PRE	ΔT_{rec}^b	τ	α	\dot{m}	y_{ign}
(#)		(MJD)	(10^{-8} erg s $^{-1}$ cm $^{-2}$)	(10^{-7} erg cm $^{-2}$)		(hours)	(s)		(10^4 g cm $^{-2}$ s $^{-1}$)	(10^8 g cm $^{-2}$)
1	101	60363.36440	2.19±0.15	2.87±0.29	N	—	13.09±2.19	—	2.29±0.17	0.83±0.14
2	102	60363.42902	2.17±0.18	2.73±0.28	Y	1.55	12.59±2.34	77.42±8.33	2.25±0.17	0.79±0.14
3	102	60363.49440	2.17±0.06	2.90±0.29	N	1.57	13.38±1.72	71.57±7.54	2.22±0.17	0.84±0.14
4	103	60363.55817	2.74±0.13	3.12±0.29	N	1.53	11.37±1.63	63.54±6.31	2.20±0.17	0.90±0.15
5	103	60363.62261	2.52±0.21	2.97±0.29	Y	1.55	11.80±2.14	65.71±6.85	2.17±0.17	0.85±0.15
6	104	60363.68849	2.29±0.19	2.73±0.26	N	1.58	11.90±2.12	70.18±7.04	2.15±0.16	0.79±0.13
7	104	60363.75415	2.32±0.21	2.49±0.22	Y	1.58	10.74±1.95	73.90±7.02	2.12±0.16	0.72±0.12
8	105	60363.82095	2.19±0.22	2.87±0.29	Y	1.60	13.11±2.69	63.67±6.83	2.10±0.16	0.83±0.14
9	105	60363.89030	2.25±0.21	2.66±0.26	N	1.66	11.82±2.25	75.14±7.80	2.08±0.16	0.77±0.13
10	106	60363.95762	2.32±0.19	3.19±0.34	N	1.62	13.72±2.57	67.51±7.57	2.06±0.16	0.92±0.16
11	106	60364.02469	2.35±0.18	3.00±0.28	N	1.61	12.81±2.21	73.62±7.29	2.05±0.16	0.87±0.14
12	107	60364.09186	2.22±0.06	2.82±0.28	N	1.61	12.69±1.59	74.53±7.77	2.03±0.15	0.81±0.14
13	108	60364.29415	2.10±0.13	2.82±0.29	Y	4.85/1.62	13.42±2.18	72.98±7.84	2.02±0.15	0.81±0.14
14	109	60364.36159	2.50±0.21	2.95±0.28	N	1.62	11.79±2.13	71.74±7.23	2.03±0.15	0.85±0.14
15	109	60364.42943	2.46±0.13	3.11±0.29	N	1.63	12.62±1.86	69.18±6.88	2.04±0.15	0.90±0.15
16	110	60364.49771	2.32±0.06	2.99±0.31	N	1.64	12.90±1.68	70.81±7.76	2.04±0.16	0.86±0.15
17	110	60364.56604	2.62±0.22	3.16±0.29	N	1.64	12.05±2.13	63.09±6.20	2.05±0.16	0.91±0.15
18	111	60364.63551	2.51±0.20	2.82±0.26	Y	1.67	11.23±1.91	69.41±6.66	2.06±0.16	0.81±0.13
19	114	60364.99047	2.47±0.22	2.87±0.28	Y	1.71	11.60±2.17	79.21±8.08	1.96±0.15	0.83±0.14
20	114	60365.06182	2.48±0.21	2.86±0.29	N	1.71	11.55±2.12	73.67±7.75	1.90±0.14	0.82±0.14
21	201	60365.13472	3.21±0.24	3.87±0.35	N	1.75	12.08±1.97	49.25±4.63	1.83±0.14	1.12±0.18
22	202	60365.28943	2.27±0.22	2.73±0.28	Y	3.71/1.85	12.02±2.38	67.74±7.18	1.66±0.13	0.79±0.14
23	204	60365.51993	2.33±0.12	2.80±0.29	N	5.53/1.84	12.05±1.87	60.53±6.60	1.50±0.11	0.81±0.14
24	204	60365.60222	2.12±0.10	2.66±0.27	N	1.98	12.59±1.87	58.67±6.16	1.49±0.11	0.77±0.13
25	205	60365.68368	2.32±0.12	2.86±0.27	N	1.96	12.32±1.81	61.06±6.08	1.49±0.11	0.83±0.14
26	207	60366.01711	2.19±0.11	2.78±0.26	N	8.00/2.00	12.67±1.82	60.81±6.10	1.58±0.12	0.80±0.13
27	209	60366.18713	2.30±0.11	3.14±0.30	N	4.08/2.04	13.67±1.96	69.09±7.00	1.63±0.12	0.90±0.15
28	209	60366.27219	2.39±0.06	3.03±0.29	Y	2.04	12.66±1.57	74.42±7.60	1.66±0.13	0.87±0.15
29	211	60366.43996	2.32±0.11	2.96±0.32	N	4.03/2.02	12.78±1.98	67.05±7.52	1.71±0.13	0.85±0.15
30	211	60366.52374	2.41±0.14	3.00±0.30	N	2.01	12.43±1.94	71.81±7.45	1.73±0.13	0.86±0.15
31	212	60366.61018	2.31±0.18	2.79±0.26	N	2.07	12.08±2.07	85.29±8.35	1.74±0.13	0.80±0.13
32	214	60366.85996	2.67±0.07	3.11±0.30	N	2.03	11.68±1.42	70.15±7.18	1.77±0.13	0.90±0.15
33	214	60366.94463	2.47±0.19	2.87±0.28	N	2.03	11.65±2.01	87.58±8.89	1.77±0.13	0.83±0.14
34	215	60367.02904	2.34±0.12	2.90±0.28	N	2.03	12.40±1.87	88.92±9.13	1.77±0.13	0.84±0.14
35	301	60367.11354	—	—	—	2.03	—	—	—	—
36	302	60367.19894	2.45±0.05	2.97±0.29	N	2.05	12.14±1.45	74.33±7.56	1.77±0.13	0.86±0.14
37	303	60367.37278	2.81±0.21	3.43±0.31	N	4.17/2.09	12.21±2.02	64.54±6.15	1.75±0.13	0.99±0.16
38	303	60367.46190	2.61±0.08	3.45±0.36	N	2.14	13.22±1.77	69.11±7.52	1.73±0.13	1.00±0.17
39	305	60367.64126	2.57±0.20	2.94±0.26	N	4.30/2.15	11.42±1.90	86.50±8.19	1.70±0.13	0.85±0.14
40	305	60367.73144	2.60±0.06	3.10±0.27	N	2.16	11.96±1.33	82.58±7.71	1.68±0.13	0.89±0.14
41	307	60367.91840	2.59±0.21	2.90±0.28	Y	2.28	11.23±2.02	89.34±9.17	1.63±0.12	0.84±0.14
42	308	60368.01282	2.66±0.06	3.04±0.30	N	2.27	11.45±1.40	76.86±8.05	1.61±0.12	0.88±0.15
43	309	60368.29469	2.69±0.20	3.12±0.29	N	2.27	11.59±1.95	63.25±6.23	1.53±0.12	0.90±0.15

Table 1 continued

Table 1 (continued)

NO.	Obs id ^a	Burst Onset	F_{peak}	f_b	PRE	ΔT_{rec}^b	τ	α	\dot{m}	y_{ign}
(#)		(MJD)	(10^{-8} erg s $^{-1}$ cm $^{-2}$)	(10^{-7} erg cm $^{-2}$)		(hours)	(s)		(10^4 g cm $^{-2}$ s $^{-1}$)	(10^8 g cm $^{-2}$)
44	309	60368.39353	2.32±0.11	3.11±0.30	N	2.37	13.41±1.92	72.02±7.35	1.50±0.11	0.90±0.15
45	309	60368.49190	—	—	—	2.36	—	—	—	—
46	310	60368.58854	2.60±0.20	2.88±0.26	N	2.32	11.10±1.82	84.09±7.89	1.44±0.11	0.83±0.13
47	311	60368.78858	2.38±0.12	2.97±0.29	N	2.56	12.47±1.81	63.50±6.42	1.38±0.10	0.86±0.14
48	313	60369.00155	2.43±0.12	2.96±0.29	N	2.55	12.19±1.78	60.80±6.15	1.32±0.10	0.85±0.14
49	314	60369.10782	2.42±0.06	2.88±0.27	N	2.55	11.91±1.38	54.62±5.31	1.29±0.10	0.83±0.14
50	314	60369.21778	2.27±0.05	2.92±0.27	Y	2.64	12.90±1.50	56.05±5.48	1.26±0.10	0.84±0.14
51	314	60369.33029	2.37±0.18	2.75±0.24	Y	2.70	11.57±1.87	60.37±5.55	1.22±0.09	0.79±0.13
52	314	60369.44306	2.53±0.19	3.02±0.27	Y	2.71	11.92±1.96	47.79±4.54	1.19±0.09	0.87±0.14
53	315	60369.55780	2.00±0.12	2.57±0.25	Y	2.75	12.85±2.02	51.21±5.31	1.16±0.09	0.74±0.13
54	316	60369.79381	2.35±0.11	2.72±0.24	N	2.81	11.60±1.58	71.44±6.65	1.10±0.08	0.78±0.12
55	317	60369.91172	2.30±0.10	2.71±0.24	Y	2.83	11.77±1.54	70.70±6.66	1.08±0.08	0.78±0.13
56	401	60371.37052	2.44±0.20	2.57±0.23	N	3.29	10.53±1.79	55.99±5.27	0.89±0.07	0.74±0.12
57	401	60371.50769	2.36±0.19	2.80±0.31	N	3.29	11.90±2.29	52.17±6.05	0.89±0.07	0.81±0.15
58	501	60373.14843	2.75±0.27	3.10±0.29	N	3.47	11.27±2.18	102.55±10.15	1.43±0.11	0.89±0.15
59	501	60373.29220	2.54±0.38	2.84±0.29	N	3.45	11.14±2.81	108.19±11.51	1.43±0.11	0.82±0.14
60	501	60373.44431	2.60±0.11	2.86±0.25	N	3.65	11.01±1.42	113.48±10.47	1.43±0.11	0.82±0.13

^a The Obs. id. starts with P061437300. We only use the last three digits to represent *Insight*-HXMT Obs. Ids..

^b The observed recurrence time. If two values are given, the second one is obtained from the measured recurrence time divided by $N + 1$, where N is the number of missed bursts.

REFERENCES

- Arnaud, K. A. 1996, in *Astronomical Society of the Pacific Conference Series*, Vol. 101, *Astronomical Data Analysis Software and Systems V*, ed. G. H. Jacoby & J. Barnes, 17
- Ballantyne, D. R., & Strohmayer, T. E. 2004, *ApJL*, 602, L105, doi: [10.1086/382703](https://doi.org/10.1086/382703)
- Bult, P., Jaisawal, G. K., Güver, T., et al. 2019, *ApJL*, 885, L1, doi: [10.3847/2041-8213/ab4ae1](https://doi.org/10.3847/2041-8213/ab4ae1)
- Chandra, A. D. 2024, *The Astronomer's Telegram*, 16471, 1
- Chen, Y.-P., Zhang, S., Zhang, S.-N., et al. 2013, *ApJL*, 777, L9, doi: [10.1088/2041-8205/777/1/L9](https://doi.org/10.1088/2041-8205/777/1/L9)
- Chen, Y.-P., Zhang, S., Zhang, S.-N., Li, J., & Wang, J.-M. 2012, *ApJL*, 752, L34, doi: [10.1088/2041-8205/752/2/L34](https://doi.org/10.1088/2041-8205/752/2/L34)
- Chen, Y. P., Zhang, S., Qu, J. L., et al. 2018, *ApJL*, 864, L30, doi: [10.3847/2041-8213/aadc0e](https://doi.org/10.3847/2041-8213/aadc0e)
- Chen, Y. P., Zhang, S., Zhang, S. N., et al. 2019, *Journal of High Energy Astrophysics*, 24, 23, doi: [10.1016/j.jheap.2019.09.001](https://doi.org/10.1016/j.jheap.2019.09.001)
- Chen, Y.-P., Shu, Z., Long, J., et al. 2022a, arXiv e-prints, arXiv:2208.12124, doi: [10.48550/arXiv.2208.12124](https://doi.org/10.48550/arXiv.2208.12124)
- Chen, Y.-P., Zhang, S., Ji, L., et al. 2022b, *ApJL*, 936, L21, doi: [10.3847/2041-8213/ac8c2c](https://doi.org/10.3847/2041-8213/ac8c2c)
- Frank, J., King, A., & Raine, D. 1992, *Accretion power in astrophysics.*, Vol. 21 (Cambridge university press)
- Galloway, D. K., & Cumming, A. 2006, *ApJ*, 652, 559, doi: [10.1086/507598](https://doi.org/10.1086/507598)
- Galloway, D. K., Cumming, A., Kuulkers, E., et al. 2004, *ApJ*, 601, 466, doi: [10.1086/380445](https://doi.org/10.1086/380445)
- Galloway, D. K., Johnston, Z., Goodwin, A., & He, C.-C. 2022, *ApJS*, 263, 30, doi: [10.3847/1538-4365/ac98c9](https://doi.org/10.3847/1538-4365/ac98c9)
- Galloway, D. K., & Keek, L. 2021, in *Astrophysics and Space Science Library*, Vol. 461, *Timing Neutron Stars: Pulsations, Oscillations and Explosions*, ed. T. M. Belloni, M. Méndez, & C. Zhang, 209–262, doi: [10.1007/978-3-662-62110-3_5](https://doi.org/10.1007/978-3-662-62110-3_5)
- Galloway, D. K., Munro, M. P., Hartman, J. M., Psaltis, D., & Chakrabarty, D. 2008, *ApJS*, 179, 360, doi: [10.1086/592044](https://doi.org/10.1086/592044)
- Galloway, D. K., Psaltis, D., Munro, M. P., & Chakrabarty, D. 2006, *ApJ*, 639, 1033, doi: [10.1086/499579](https://doi.org/10.1086/499579)
- Goodwin, A. J., Heger, A., & Galloway, D. K. 2019, *ApJ*, 870, 64, doi: [10.3847/1538-4357/aaeed2](https://doi.org/10.3847/1538-4357/aaeed2)

- Guichandut, S., & Cumming, A. 2023, in AAS/High Energy Astrophysics Division, Vol. 20, AAS/High Energy Astrophysics Division, 116.11
- Guo, C.-C., Liao, J.-Y., Zhang, S., et al. 2020, *Journal of High Energy Astrophysics*, 27, 44, doi: [10.1016/j.jheap.2020.02.008](https://doi.org/10.1016/j.jheap.2020.02.008)
- Illiano, G., Coti Zelati, F., Marino, A., et al. 2024, *The Astronomer's Telegram*, 16510, 1
- Ji, L., Ge, M., Chen, Y., et al. 2024, *ApJL*, 966, L3, doi: [10.3847/2041-8213/ad3c29](https://doi.org/10.3847/2041-8213/ad3c29)
- Ji, L., Zhang, S., Chen, Y., et al. 2013, *MNRAS*, 432, 2773, doi: [10.1093/mnras/stt625](https://doi.org/10.1093/mnras/stt625)
- Keek, L., Ballantyne, D. R., Kuulkers, E., & Strohmayer, T. E. 2014, *ApJL*, 797, L23, doi: [10.1088/2041-8205/797/2/L23](https://doi.org/10.1088/2041-8205/797/2/L23)
- Kuulkers, E., den Hartog, P. R., in't Zand, J. J. M., et al. 2003, *A&A*, 399, 663, doi: [10.1051/0004-6361:20021781](https://doi.org/10.1051/0004-6361:20021781)
- Lewin, W. H. G., & van der Klis, M. 2006, *Compact Stellar X-ray Sources*
- Lewin, W. H. G., van Paradijs, J., & Taam, R. E. 1993, *SSRv*, 62, 223, doi: [10.1007/BF00196124](https://doi.org/10.1007/BF00196124)
- Li, Z., De Falco, V., Falanga, M., et al. 2018, *A&A*, 620, A114, doi: [10.1051/0004-6361/201833857](https://doi.org/10.1051/0004-6361/201833857)
- Li, Z., Kuiper, L., Falanga, M., et al. 2024, *The Astronomer's Telegram*, 16548, 1
- Liao, J.-Y., Zhang, S., Chen, Y., et al. 2020, *Journal of High Energy Astrophysics*, 27, 24, doi: [10.1016/j.jheap.2020.02.010](https://doi.org/10.1016/j.jheap.2020.02.010)
- Liu, C., Zhang, Y., Li, X., et al. 2020, *Science China Physics, Mechanics, and Astronomy*, 63, 249503, doi: [10.1007/s11433-019-1486-x](https://doi.org/10.1007/s11433-019-1486-x)
- Lu, Y., Li, Z., Yu, W., Pan, Y., & Falanga, M. 2024, *ApJ*, 969, 15, doi: [10.3847/1538-4357/ad4d86](https://doi.org/10.3847/1538-4357/ad4d86)
- Lu, Y., Li, Z., Pan, Y., et al. 2023, *A&A*, 670, A87, doi: [10.1051/0004-6361/202244984](https://doi.org/10.1051/0004-6361/202244984)
- Molkov, S. V., Lutovinov, A. A., Tsygankov, S. S., et al. 2024, arXiv e-prints, arXiv:2404.19709, doi: [10.48550/arXiv.2404.19709](https://doi.org/10.48550/arXiv.2404.19709)
- Negoro, H., Mihara, T., Serino, M., et al. 2024, *The Astronomer's Telegram*, 16483, 1
- Ng, M., Ray, P. S., Sanna, A., et al. 2024, *ApJL*, 968, L7, doi: [10.3847/2041-8213/ad4edb](https://doi.org/10.3847/2041-8213/ad4edb)
- Papitto, A., Di Marco, A., Poutanen, J., et al. 2024, arXiv e-prints, arXiv:2408.00608, doi: [10.48550/arXiv.2408.00608](https://doi.org/10.48550/arXiv.2408.00608)
- Ray, P. S., Strohmayer, T. E., Sanna, A., et al. 2024, *The Astronomer's Telegram*, 16480, 1
- Sanchez-Fernandez, C., Kuulkers, E., Ferrigno, C., Chenevez, J., & Del Santo, M. 2024, *The Astronomer's Telegram*, 16507, 1
- Sguera, V., & Sidoli, L. 2024, *The Astronomer's Telegram*, 16493, 1
- Speicher, J., Ballantyne, D. R., & Fragile, P. C. 2024, *ApJ*, 976, 44, doi: [10.3847/1538-4357/ad863d](https://doi.org/10.3847/1538-4357/ad863d)
- Takeda, T., Ota, N., Watanabe, S., et al. 2024, *The Astronomer's Telegram*, 16495, 1
- Wang, P. J., Chen, Y. P., Ji, L., et al. 2024, *A&A*, 689, A47, doi: [10.1051/0004-6361/202348352](https://doi.org/10.1051/0004-6361/202348352)
- Worpel, H., Galloway, D. K., & Price, D. J. 2013, *ApJ*, 772, 94, doi: [10.1088/0004-637X/772/2/94](https://doi.org/10.1088/0004-637X/772/2/94)
- . 2015, *ApJ*, 801, 60, doi: [10.1088/0004-637X/801/1/60](https://doi.org/10.1088/0004-637X/801/1/60)
- Yu, W., Li, Z., Lu, Y., et al. 2024, *A&A*, 683, A93, doi: [10.1051/0004-6361/202348195](https://doi.org/10.1051/0004-6361/202348195)
- Zhang, S. N. 2007, *Highlights of Astronomy*, 14, 41, doi: [10.1017/S1743921307009842](https://doi.org/10.1017/S1743921307009842)
- Zhang, S. N., Cui, W., Chen, W., et al. 2000, *Science*, 287, 1239, doi: [10.1126/science.287.5456.1239](https://doi.org/10.1126/science.287.5456.1239)
- Zhang, S.-N., Li, T., Lu, F., et al. 2020, *Science China Physics, Mechanics, and Astronomy*, 63, 249502, doi: [10.1007/s11433-019-1432-6](https://doi.org/10.1007/s11433-019-1432-6)
- Zhao, G., Li, Z., Pan, Y., et al. 2022, *A&A*, 660, A31, doi: [10.1051/0004-6361/202142801](https://doi.org/10.1051/0004-6361/202142801)